

Constraining the atmosphere of GJ 1214b using an optimal estimation technique

J. K. Barstow,^{1,2}★ S. Aigrain,¹ P. G. J. Irwin,² L. N. Fletcher² and J.-M. Lee^{2,3}

¹Department of Astrophysics, Denys Wilkinson Building, University of Oxford, Oxford OX1 3RH, UK

²Atmospheric, Oceanic and Planetary Physics, Clarendon Laboratory, University of Oxford, Oxford OX1 3PU, UK

³Institute for Theoretical Physics, University of Zürich, CH-8057 Zürich, Switzerland

Accepted 2013 June 27. Received 2013 June 20; in original form 2013 April 26

ABSTRACT

We explore cloudy, extended H₂–He atmosphere scenarios for the warm super-Earth GJ 1214b using an optimal estimation retrieval technique. This planet, orbiting an M4.5 star only 13 pc from the Earth, is of particular interest because it lies between the Earth and Neptune in size and may be a member of a new class of planet that is neither terrestrial nor gas giant. Its relatively flat transmission spectrum has so far made atmospheric characterization difficult. The Non-linear optimal Estimator for MultivariateE spectral analysis (NEMESIS) algorithm is used to explore the degenerate model parameter space for a cloudy, H₂–He-dominated atmosphere scenario. Optimal estimation is a data-led approach that allows solutions beyond the range permitted by *ab initio* equilibrium model atmosphere calculations, and as such prevents restriction from prior expectations. We show that optimal estimation retrieval is a powerful tool for this kind of study, and present an exploration of the degenerate atmospheric scenarios for GJ 1214b. Whilst we find a family of solutions that provide a very good fit to the data, the quality and coverage of these data are insufficient for us to more precisely determine the abundances of cloud and trace gases given an H₂–He atmosphere, and we also cannot rule out the possibility of a high molecular weight atmosphere. Future ground- and space-based observations will provide the opportunity to confirm or rule out an extended H₂–He atmosphere, but more precise constraints will be limited by intrinsic degeneracies in the retrieval problem, such as variations in cloud top pressure and temperature.

Key words: radiative transfer – methods: data analysis – planets and satellites: atmospheres.

1 INTRODUCTION

In recent years, the discovery of exoplanets in close-by systems has allowed the first attempts at characterizing their atmospheres. Planets with a high planet:star surface area ratio are the most favourable targets, and the super-Earth-sized planet orbiting the M4.5 star GJ 1214, only 13 pc distant from the Earth, is one such case. This planet is of particular interest because it lies between the Earth and Neptune in size, meaning that there is no Solar system analogue and so it may be a member of a new class of planet that is neither terrestrial nor gas giant.

GJ 1214b was discovered in 2009 (Charbonneau et al. 2009) by the MEarth project (Irwin et al. 2009), a survey designed to detect any transits occurring within a sample of 2000 nearby M dwarf stars. Radial velocity data were obtained subsequently with the High Accuracy Radial velocity Planet Search instrument, confirming the planetary nature of the transiting object and placing a constraint on

its mass. It was found to have a radius of $2.68 \pm 0.13R_{\oplus}$ and a mass of $6.55 \pm 0.98M_{\oplus}$; these estimates were subsequently recalculated by Høst et al. (2013) but both sets of values were found to be in good agreement within the error bars. The planet’s calculated density indicates that its composition lies somewhere between a ‘water-world’ and a ‘mini-Neptune’, and its equilibrium temperature is expected to be around 550 K assuming a low Bond albedo or 400 K with a Bond albedo of 0.75 (Charbonneau et al. 2009). Because its density is compatible with a range of bulk compositions, constraining the atmospheric composition for GJ 1214b is a crucial step towards understanding its formation process and history.

The technique of transit spectroscopy (Coustenis et al. 1997; Seager & Sasselov 2000) has been used with some success to draw inferences about the atmospheres of hot Jupiter-sized planets such as HD 189733b and HD 209458b (e.g. Knutson et al. 2008; Sing et al. 2008; Swain et al. 2009; Pont et al. 2013). The absorbing species in a planet’s atmosphere can be identified by observing the transit over a range of wavelengths; the presence of an absorber is indicated by a deeper reduction in flux at the location of absorption features. The shape and size of these features provide information

★ E-mail: j.barstow1@physics.ox.ac.uk

about the atmospheric scale height, volume mixing ratio (VMR) of absorbers and the presence of cloud or aerosol species. Further information can be obtained when the planet is eclipsed by the star; the difference between in and out of transit fluxes at each wavelength gives the emission spectrum of the planet's dayside, which as well as providing information about absorbing gases can place constraints on the temperature structure (Lee, Fletcher & Irwin 2012).

This technique has also been applied to GJ 1214b, using a wide range of ground- and space-based instruments. GJ 1214b is too cool for its thermal emission relative to the stellar flux to be observed with currently available telescopes (Miller-Ricci & Fortney 2010), so these observations have been confined to measurements of transmission through the atmosphere in primary transit. The combined efforts of several groups have yielded a fairly continuous spectrum between 0.4 and 5 μm , making GJ 1214b one of the best-studied exoplanets; however, the interpretation of this spectrum has proved challenging due to a lack of significant features (Bean, Miller-Ricci Kempton & Homeier 2010; Bean et al. 2011; Berta et al. 2012; de Mooij et al. 2012).

The flatness of the spectrum has led to the formulation of two competing atmospheric models. The first, favoured by Bean et al. (2011), Désert et al. (2011) and Berta et al. (2012), is a planet with a high molecular weight atmosphere. All these authors produce synthetic spectra based on an atmosphere with varying proportions of H_2 , He and H_2O , with models containing more than 50 per cent H_2O providing the best fit to the data. An atmosphere with high molecular weight has a small atmospheric scale height, which acts to reduce the size of absorption features seen in transmission. The second model is a planet with a roughly solar composition atmosphere (mostly H_2 and He with trace amounts of other species) but with an opaque haze or cloud layer at high altitude that prevents transmission through the atmosphere in between molecular absorption bands and so masks expected features (Miller-Ricci Kempton, Zahnle & Fortney 2012; de Mooij et al. 2012; Howe & Burrows 2012). The most exhaustive range of models is provided by Howe & Burrows (2012). Three of their five best-fitting models are H_2 –He atmospheres with different sizes of hydrocarbon haze particles, based on chemicals called ‘tholins’ that are found on Saturn’s moon Titan, and the others are N_2 – H_2O -dominated atmospheres that produce flat spectra because of their high molecular weight. Similar results are presented by Morley et al. (2013); they use an *ab initio* modelling technique to produce photochemical hydrocarbon hazes in both solar metallicity and enhanced metallicity models, and they find that hydrocarbon hazes can produce a good fit to the data in an enhanced metallicity (50 \times solar) model without the introduction of any other scattering cloud species. An extinction-only approximation was adopted for the scattering behaviour of the particles.

The attempts by the above authors to fit the spectrum of GJ 1214b have been undertaken by comparing a range of synthetic spectra generated from chemically and thermally likely model atmospheres to the data, and calculating a goodness of fit parameter for each. This ‘bottom-up’ approach is useful because of its reliance on known physics of planetary atmospheres, but exoplanets like GJ 1214b exist in regimes outside our current experience, so the assumptions that go into these atmospheric models may be incorrect in this case. Even for Solar system planets, observations can be very far from scenarios predicted by thermal and photochemical equilibrium models. For example, Atreya et al. (2005) state that extremely patchy ammonia cloud coverage on Jupiter seen in data from the Galileo satellite is at odds with the global coverage expected from

cloud physics models; they suggest that spectral signatures of expected cloud components may be masked by other hazes. Therefore, it is worth considering solutions from a data-led approach – optimal estimation. This approach, described in more detail in Section 3, makes fewer assumptions about the nature of the atmosphere and so can find atmospheric solutions that fit the data but might be excluded by too-stringent assumptions in *ab initio* approaches.

This paper makes use of the available spectroscopic data to investigate what constraint, if any, it is possible to place on GJ 1214b’s atmosphere using the optimal estimation technique previously presented by Lee et al. (2012). The sources and treatment of the data are discussed in Section 2; the method and model are briefly described in Section 3; the atmospheric models that produce the best fit to the spectrum are presented in Section 4, and in Section 5 we investigate the degeneracy and reliability of this solution, and the improvement we expect from future observations.

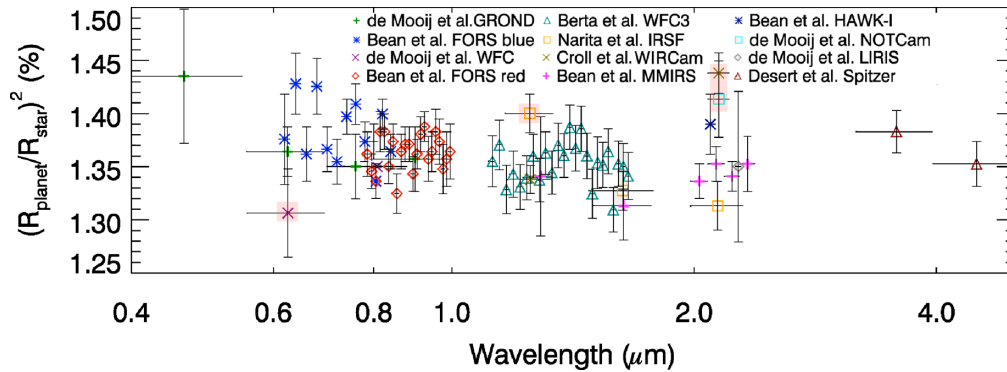
2 SPECTROSCOPIC DATA

The analysis of GJ 1214b is complicated by the fact that the data come from several different sources and were obtained at different times, as has been found by e.g. Bean et al. (2011). The sources of data, wavelength ranges, instruments used and any modifications to the errors are listed in Table 1.

Upon plotting these data, it becomes immediately apparent that measurements made in the same part of the spectrum by different instruments are not compatible within the error bars (Fig. 1). This is clearly a problem when trying to find an atmospheric model that produces a good fit to the spectrum; for example, Bean et al. (2011) shift all the VLT/FORS blue data points down by a constant factor to make them more comparable to the VLT/FORS red points, whereas Berta et al. (2012) do not do this in their analysis. In this work, rather than artificially shift any of the data, we have chosen to increase the error bars on some points from the estimates provided in the original papers. This ensures that measurements made in the same wavelength ranges with different instruments are compatible within the error bars. Based on the decision of Bean et al. (2011) to shift the FORS blue data to match FORS red, we have increased the error bars of all the FORS data by a factor of 1.5; this makes the overlapping points more comparable. We have also increased the errors on some of the broader band measurements: the Isaac Newton Telescope (INT)/Wide Field Camera (WFC) point measured by de Mooij et al. (2012) in the *r* band, which has a poor light-curve fit, to ensure compatibility with the ESO 2.2-m telescope Gamma-Ray burst Optical/Near-infrared Detector (GROND) result presented in the same paper and the Bean et al. (2011) FORS blue results; the *J*-band point measured by Narita et al. (2012) to bring it more in line with the Berta et al. (2012) *Hubble Space Telescope* (HST)/WFC3 data; the Nordic Optical Telescope NOTCam and Canada–French–Hawaii Telescope/WIRCam Ks points, which are much higher than the Magellan/MMT and Magellan InfraRed Spectrograph (MMIRS), VLT/HAWK-I and InfraRed Survey Facility (IRSF)/Simultaneous 3-colour InfraRed Imager for Unbiased Survey (SIRIUS) values at the same wavelength. All these errors are also increased by a factor of 1.5, except that of the Croll et al. (2011) WIRCam Ks point which is increased by a factor of 3 since it seems to be an extreme outlier when compared with other data. Increasing the error on data that appear to be less reliable means that these points are given less weight by the retrieval algorithm, to ensure that the solution is driven by more robust observations.

Table 1. Sources of spectroscopic data for GJ 1214b.

Author	Instrument	Wavelength range	Error increase
Bean et al. (2010)	VLT/FORS red	0.78–1.0 μm	1.5 \times
Bean et al. (2011)	VLT/FORS blue	0.61–0.85 μm	1.5 \times
	Magellan/MMIRS	J, H, K	None
	VLT/HAWK-I	K	None
Désert et al. (2011)	<i>Spitzer</i> /IRAC	3.6, 4.5 μm	None
Croll et al. (2011)	Canada–French–Hawaii Telescope/WIRCam	J, Ks	3 \times (Ks)
de Mooij et al. (2012)	MPI-ESO 2.2 m/GROND	g, r, i, z	None
	INT/WFC	r, I	1.5 \times (r)
	Nordic Optical Telescope/NOTCam	Ks	1.5 \times
	William Herschel Telescope/LIRIS	Kc	None
Berta et al. (2012)	<i>HST</i> /WFC3	1.3–1.6 μm	None
Narita et al. (2012)	IRSF/SIRIUS	J, H, K	1.5 \times (J)

**Figure 1.** The spectroscopic data available for GJ 1214b from different instruments. It can be seen that the FORS blue and red data appear to disagree with each other in the region of overlap, and the WFC r, IRSF J, and WIRCam and NOTCam Ks points are outliers (shaded in red). The error bars shown here are as given in the literature.

Increasing the error bars is of course not the only way of accounting for the intrinsic disagreements within the GJ 1214b data set (e.g. the method of Bean et al. 2011, as mentioned above) and we explore other possibilities in Section 5.1. This is a good test of the robustness of our result in relation to the uncertainties inherent in the combination of sparse, temporally separated spectroscopic and photometric measurements. If the only systematics present are offsets between measurements from different instruments, then the method adopted here may risk lowering the significance of certain features within a given spectroscopic data set unnecessarily; however, since we do not know the form of any potential systematics at this stage, we feel that this approach is reasonable in light of the tests described in Section 5.1.

GJ 1214b was originally classified as an inactive M dwarf by Hawley, Gizis & Reid (1996), but subsequently Kundurthy et al. (2011) have seen hints of spot crossing events and Murgas et al. (2012) see photometric dispersion in $H\alpha$ transit light curves, both of which provide tentative evidence for stellar activity. However, Berta et al. (2011) find that significant effects on transmission spectra from stellar activity are unlikely given the current level of precision on existing data; it is likely to become important for future observations with higher signal-to-noise ratio. Whilst de Mooij et al. (2012) consider the effect of unocculted star spots to be potentially important, they conclude that this is not a suitable explanation for the observed increase in planetary radius in the g and K_s bands. We cannot rule out the possibility that periods of high activity may be responsible for the discrepancies between different observations,

but without detailed information about activity levels increasing the error bars on these points is the most appropriate way to account for the effect. Stellar activity monitoring and starspot correction of the kind performed for HD 189733b (Pont et al. 2013) will have a crucial role in future observation of GJ 1214b.

3 THE RETRIEVAL METHOD

3.1 NEMESIS

NEMESIS, the Non-linear optimal Estimator for Multivariate spectral analysis (Irwin et al. 2008), was originally developed to analyse remote sensing data from Solar system planets collected by orbiters such as Cassini and Venus Express as well as ground-based telescope facilities. More recently, it has been modified to allow the simulation of primary transit and secondary eclipse spectra for extrasolar planets (Lee et al. 2012). Its track record in Solar system studies (Tsang et al. 2010; Irwin et al. 2011; Barstow et al. 2012; Cottini et al. 2012), versatility and efficient approach to radiative transfer calculation make it a useful and reliable tool for exoplanet science. NEMESIS uses the correlated- k approximation (Goody & Yung 1989; Lacis & Oinas 1991), which allows absorption coefficients over a spectral interval to be pre-tabulated, to rapidly calculate synthetic spectra based on model atmosphere parameters. Whilst it relies on the assumption that absorption line strengths are well-correlated between model atmospheric layers, i.e. lines that are strongest in the lowest atmospheric layer are also strong in the

layer above, the approach significantly reduces computation time over the line-by-line method. Comparisons with line-by-line calculations show that the correlated- k approximation is sufficiently accurate for planetary atmospheric modelling (Irwin et al. 2008).

The fast forward model calculation is coupled with an optimal estimation scheme based on the approach of Rodgers (2000). The user provides NEMESIS with an initial atmospheric state and an associated error on each of the parameters to be varied – the a priori solution – which acts to prevent overfitting and stops retrieval solutions from becoming unphysical. To ensure that a global solution is found, the retrieval should be performed for a range of different a priori values; if the solution is global and non-degenerate, it should be the same regardless of the initial atmospheric state. NEMESIS then calculates a synthetic spectrum from this initial state, and the difference between the measured spectrum and this synthetic. It also calculates the derivative of the spectrum with respect to each of the variable parameters in the model, which allows an efficient exploration of the parameter space. The best-fitting solution is found by iterating from the a priori solution until the cost function, which represents the difference between the measured and synthetic spectra together with the deviation from the a priori solution, is minimized. For further details about the structure of NEMESIS and its use for retrievals of extrasolar planet atmospheres, see Irwin et al. (2008) and Lee et al. (2012).

There are six independent variables in our retrieval of GJ 1214b. We include two populations of cloud particles and vary the total optical depth of each; we also retrieve altitude-invariant VMRs for H₂O, CO₂ and CH₄, and the radius of the planet at the 10-bar level. This last parameter is necessary because the radius quoted in the literature is derived from white light transit observations and is simply the radius at which the atmosphere becomes opaque to white light, which is dependent on the atmospheric properties. When the VMRs of the active gases change in the retrieval, the VMRs of the H₂ and He that make up the rest of the atmosphere are scaled (with a fixed ratio of 0.85:0.13) to ensure the sum of the VMRs is unity.

To investigate the sensitivity of the retrieval to the chosen a priori solution (given in Table 2), we follow a ‘bracketed retrieval’ procedure. For each of the model parameters except the radius, which effectively just scales the final result, we use 21 different starting points spanning 4 orders of magnitude and perform the

retrieval for each of these 21 starting points. This means we run the retrieval a total of 105 times, varying the a priori for only one parameter at a time. See Section 3.2 for further details of the a priori choice. A reduced χ^2 parameter¹ is calculated in each case, with a good fit being where the reduced χ^2 is close to 1. This process tests the sensitivity to the a priori and the reliability of the best-fitting solution.

3.2 Atmospheric model

The advantage of the optimal estimation approach is that, if there is sufficient information available in a spectrum to constrain atmospheric properties, the a priori atmospheric state should not affect the result (Irwin et al. 2008). The a priori atmospheric state we assume here is based on the best-fitting models of Howe & Burrows (2012). Howe & Burrows (2012) demonstrate that it is possible to produce a fit of comparable quality to a high-molecular-weight model atmosphere by adding tholin haze particles to an H₂–He model atmosphere, but their models do not successfully simultaneously fit both the slight slope in the blue part of the spectrum (0.5–0.8 μm ; see Fig. 1) and the flatter infrared region (longwards of 0.8 μm).

3.2.1 Clouds

Howe & Burrows (2012) use models with different sizes of tholin haze particle, but they only include one size in each separate model. Cloud particle extinction is maximized in the Mie scattering regime, where the particle size is comparable to the wavelength of light, so in order to fit the apparent increase in extinction towards the blue end of the spectrum and the fairly constant extinction throughout the infrared a range of particle sizes is required. We therefore adopt a two-mode cloud model: a very narrow size distribution of 0.1- μm -sized particulate haze (‘cloud 1’) and a broader lognormal distribution of larger particles with a modal radius of 1 μm and a width of 0.25 (‘cloud 2’). The narrowness of the 0.1 μm haze size distribution means that the extinction efficiency decreases throughout the visible, producing the blue–red downward slope in the transmission spectrum, whilst the broader size distribution in cloud 2 allows absorption over a broader range of wavelengths in the infrared as the extinction efficiency does not decrease as rapidly with wavelength. We use tholin refractive index data from Khare et al. (1984). This kind of multi-modal cloud model has been used to successfully model the Venusian sulphuric acid haze and cloud (e.g. Crisp 1986; Grinspoon et al. 1993; Pollack et al. 1993).

It is of course possible that any clouds on GJ 1214b would be made of something other than tholins; however, in this model we adopt a single scattering approximation, which means that the main variable affecting the amount of light scattered by the cloud is just the size of the cloud particle and not what it is made of. de Kok & Stam (2012) point out that this approximation is not valid where particles are highly forward or backward scattering, but given the large error bars on the GJ 1214b spectrum we expect any uncertainty from scattering assumptions to be second order. Tholins are also a logical choice of cloud constituent where the optical depth is allowed to vary freely, because they are made of hydrocarbons and H and C are widely available in a solar composition atmosphere.

Table 2. Initial number densities of cloud species (number per gram of atmosphere) and VMRS of spectrally active gases (ppmv). The cloud abundances translate to 5600 0.1- μm particles per cm^3 and 5.6 larger particles per cm^3 at the cloud base pressure of 100 mbar, which then decreases with the atmospheric pressure scale height towards higher altitudes. The gas VMRs are assumed to be constant with altitude.

Variable	Value
Cloud 1	10^9
Cloud 2	10^6
H ₂ O VMR	1000
CO ₂ VMR	100
CH ₄ VMR	500

¹ The reduced χ^2 is the χ^2 goodness-of-fit parameter divided by the number of degrees of freedom (number of spectral points – number of model variables – 1).

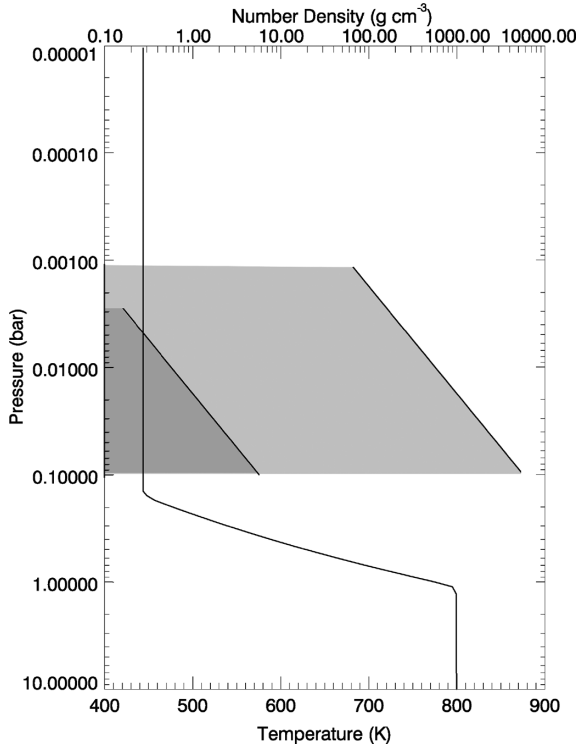


Figure 2. The model temperature profile for GJ 1214b, plus a priori number densities for the 0.1 μm haze (light grey) and 1 μm cloud (dark grey), all as a function of pressure. The model atmosphere extends up to 10^{-12} bar, but because it is isothermal above 0.1 bar the upper atmosphere is not shown in this plot.

Other likely constituents in the GJ 1214b temperature range are ZnS and KCl (Morley et al. 2012, 2013), but the solar abundances of the metals restrict the maximum cloud optical depth that can be achieved.

We also do not allow the vertical positioning of the cloud to vary in our nominal model. After Howe & Burrows (2012), we place the cloud in the pressure range 1–100 mbar; the second cloud population with larger particles only extends up to 3 mbar altitude as we would not expect larger particles to be supported up to the same altitude as the smaller haze (e.g. as on Venus). The a priori cloud number densities are shown in Fig. 2. We test the effect of varying the vertical positioning of the cloud in Section 5.2 by repeating the retrieval with a model cloud top at three different altitudes and comparing the results.

3.2.2 Gases

We adopt a bulk H_2 –He atmospheric model, as Howe & Burrows (2012), with trace amounts of H_2O , CO_2 and CH_4 . We restrict ourselves to these few species as they are the most spectrally active in the region of interest out of the common molecules we expect to occur. These are also the mini-Neptune scenario constituents adopted by Benneke & Seager (2012) in their paper detailing observations of a GJ 1214b-like atmosphere with the *James Webb Space Telescope*. We include CH_4 but not CO because CH_4 should be far more abundant than CO in GJ 1214b due to its temperature (Lodders & Fegley 2002). The sources of the absorption data for these three gases are listed in Table 3. We also include H_2 –He collision-induced absorption as in Lee et al. (2012).

Table 3. Sources of gas absorption line data.

Gas	Source
H_2O	HITEMP2010 (Rothman et al. 2010)
CO_2	CDS-1000 (Tashkun et al. 2003)
CH_4	STDS (Wenger & Champion 1998)

Due to the flatness of the spectrum, only upper limits on the VMRs of H_2O , CO_2 and CH_4 are likely to be achievable, as this means that the signal-to-noise ratio on the variation of the spectrum with wavelength is small.

3.2.3 Temperature structure

The temperature structure of GJ 1214b is not known, nor is there enough information in the transmission spectrum to independently constrain it along with all the other possible variables (Barstow et al. 2013). It is therefore necessary to use an estimated temperature profile in the atmospheric model. Whilst there is not enough information to independently constrain the temperature, changes in the temperature structure do nonetheless affect the transmission spectrum because the atmospheric scale height depends on the temperature – increasing the temperature increases the scale height, and vice versa. However, increasing the planetary radius would produce the same effect on the spectrum as increasing the temperature, because it lowers the gravitational acceleration of the planet which also increases the scale height (Barstow et al. 2013). Any inaccuracies in our temperature estimation will therefore be compensated for to some extent in the radius retrieval and so should not significantly affect the result. This hypothesis is tested in Section 5.3. GJ 1214b may be tidally locked as it is close to its parent star (~ 0.01 au), meaning that equilibrium temperature estimates are not necessarily valid for the terminator regions, so this is another reason for testing the sensitivity of the retrieval to the estimated temperature profile.

The temperature structure we adopt is arrived at using the estimation process described in Barstow et al. (2013), and is shown here in Fig. 2. The stratospheric temperature is calculated based on an assumed equilibrium temperature of 530 K, towards the higher end of the range indicated by Charbonneau et al. (2009), corresponding to a Bond albedo of 0.15. We explore the effect of varying the stratospheric temperature in Section 5.3. As in Barstow et al. (2013), we assume the presence of an adiabat between 1 and 0.1 bar, and we use the specific heat capacities c_p for H_2 and He at the stratospheric temperature, as they do not vary greatly over the temperature range in the model profile. The deep atmospheric temperature is calculated using equation 1:

$$T_{\text{trop}} = T_{\text{strat}} - \frac{kT_{\text{strat}}}{mc_p} \ln \left(\frac{p_1}{p_2} \right), \quad (1)$$

where k is the Boltzmann constant, T_{strat} is the stratospheric temperature and m is the molecular mass of the atmosphere. p_1 and p_2 are pressures at the top and bottom of the adiabat.

Whilst we have explained the derivation of a temperature profile with an adiabatic troposphere, even in a cloud-free atmosphere no signal will be observed from pressure levels deeper than 0.1 bar in transmission (Barstow et al. 2013); the details of the temperature profile below this are therefore relatively unimportant, so it is the isothermal stratospheric temperature that we expect to have the largest effect on the retrieval.

4 RESULTS

Our best-fitting spectrum to the available GJ 1214b data is presented in Fig. 3. We show it both integrated at the resolution of the individual observation bands and at a resolving power of 300. It can be seen that there are a series of clear molecular absorption features between 2 and 5 μm , which the currently available data do not probe in detail. If these features could be observed a much stronger constraint on the atmosphere would be obtained.

The optimal values of the model parameters and associated errors are presented in Table 4. It can be seen that the error bars on these values are very large, because they represent a weighted average over each retrieval run in the bracketed retrieval test described in Section 3.1. The weighting used in this case is the calculated reduced χ^2 , with larger χ^2 values being given less weight since those models produce a poorer fit to the spectrum.

The full results of the bracketed retrieval test are shown in Figs 4–8. For each test, the variations in the retrieved values for each variable are shown, along with the synthetic spectra produced from each retrieval run. The colours correspond to the reduced χ^2 , with the red point in each plot having the highest χ^2 and the black point the lowest. In general, however, the variation in χ^2 is not very great and there are few models which give a fit with a reduced χ^2 significantly greater than 1. Several combinations of model parameters produce an equally good fit to the spectrum, with some values varying over several orders of magnitude, indicating that this problem is highly degenerate; this is also clear from Fig. 9, which shows the correlation between the different retrieval variables. The only variables that do not show significant (magnitude >2.5) correlation with another are the H_2O and CO_2 VMR; cloud 1 optical depth is positively correlated with cloud 2 optical depth and CH_4 VMR, and the radius is negatively correlated with cloud optical depths and CH_4 VMR. The high correlations are indicative of degeneracy between different model atmosphere scenarios; for example, increasing the cloud optical depths increases the opacity of the atmosphere at higher altitudes, making the planet appear bigger, but this effect can be compensated for if the radius at 10 bar is decreased. This means that a large range of cloudy model atmospheres is plausible, which is similar to the result of Morley et al. (2013), who also find that several models containing hydrocarbon hazes provide an adequate fit to the data.

It is also clear in Figs 4–8 that in the majority of cases the retrieval is being driven by the chosen a priori rather than by information in the measured spectrum, as the retrieved parameters are clearly correlated with the a priori. This is particularly severe for cloud 2, H_2O

Table 4. The parameter values in the best-fitting model; all are expressed as multiplying factors on the model values listed in Table 2, except the radius which is in km. For the multiplying factors, the error given is the error in the logarithm.

Variable	Value	Error
Cloud 1	1.55	1.00
Cloud 2	0.783	1.13
H_2O VMR	1.16	1.04
CO_2 VMR	0.876	1.16
CH_4 VMR	0.169	0.732
10-bar radius	15320 km	58 km

and CO_2 , where the correlation is almost linear. We cannot therefore draw any reliable conclusion from these retrieval results, although likely values for the model parameters are indicated. We also find that a straight line can fit the available data with a reduced χ^2 of 0.94, and therefore we cannot claim to have detected the presence of any molecular species on GJ 1214b. GJ 1214b is insufficiently dense to be a rocky, atmosphere-less planet, so we do not expect that a straight line represents a realistic, physical scenario, but this fact demonstrates the limitations of the current data set.

The retrieved H_2O VMR shows almost a 1:1 correspondence with the a priori value (Fig. 6), making it impossible to trust the retrieval for this variable. This is because of the trade-off of two different effects governing the size of the H_2O absorption features; increasing the abundance of H_2O not only increases the absorption due to this gas (features look larger), but it also increases the molecular weight and therefore reduces the scale height of the atmosphere (features look smaller). A range of H_2O VMRs spanning 4 orders of magnitude is compatible with the observations, and it has already been shown by several authors (Bean et al. 2011; Désert et al. 2011; Berta et al. 2012) that even higher abundances of H_2O are compatible with the data. It is clearly not possible to place a meaningful constraint on the abundance of H_2O in GJ 1214b's atmosphere with the data currently available. This is similarly true of the CO_2 abundance; whilst there is no significant degeneracy between CO_2 abundance and other parameters, there is clearly a strong dependence on the a priori (Fig. 7). We can infer from this that the spectrum is not strongly affected by the presence of CO_2 in the model atmosphere since variations in CO_2 abundance do not affect the retrieval of

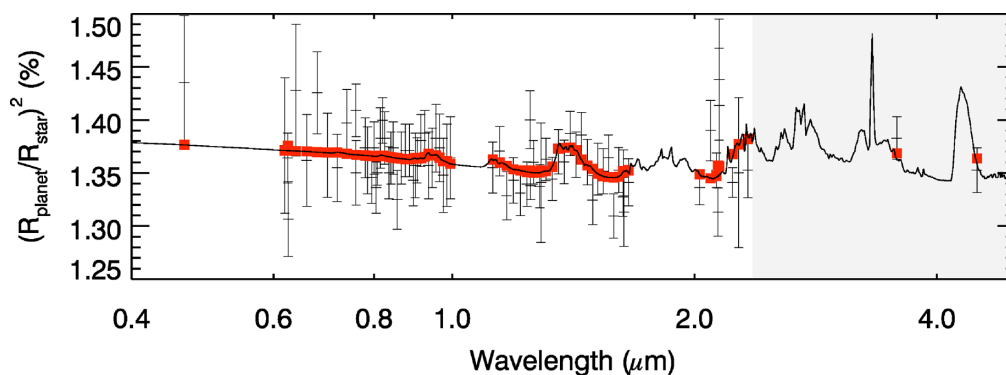


Figure 3. Best-fitting spectrum for GJ 1214b, based on the NEMESIS bracketed retrievals. The black points with error bars are the data, the red squares are the best-fitting synthetic spectrum convolved with the filter functions for each data point, and the black line is the best-fitting spectrum at $R = 300$. The highlighted region shows features in a currently data-poor part of the spectrum that may help to distinguish between different scenarios.

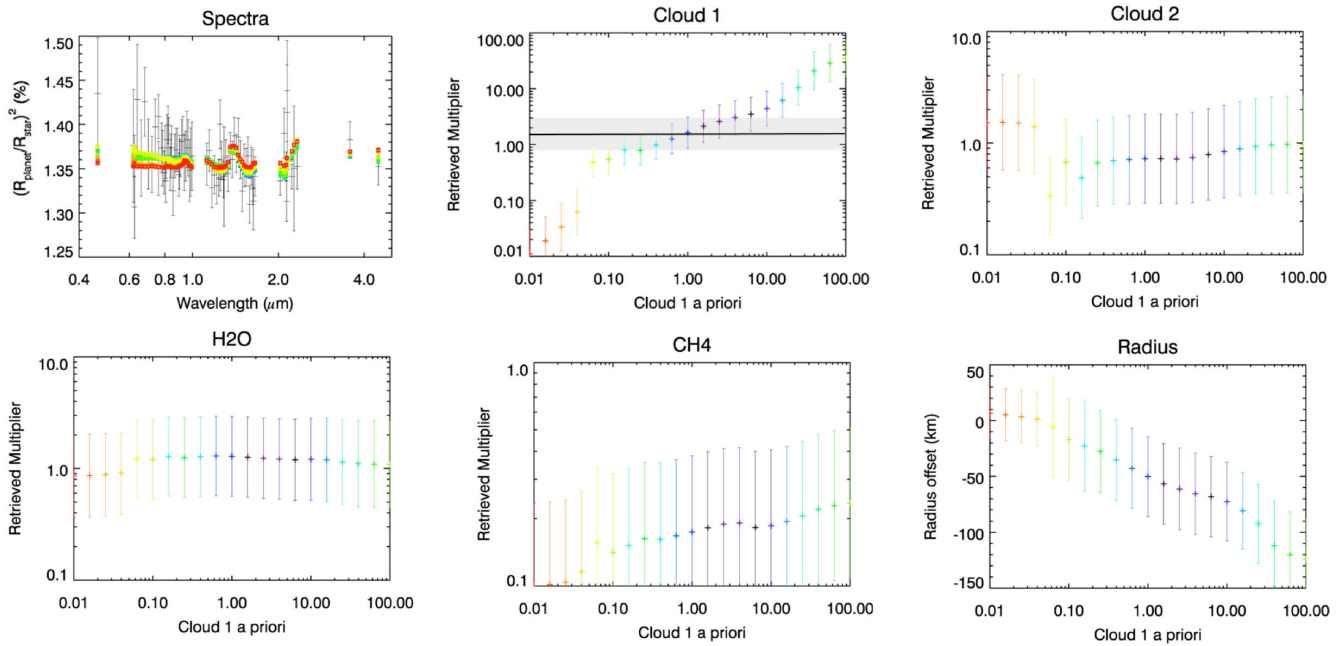


Figure 4. Bracketed retrieval results for GJ 1214b, where the a priori being altered is the cloud 1 number density. We do not plot the results for CO₂ as the retrieved values do not vary significantly for different a priori scenarios. The different colours correspond to different values of the reduced χ^2 , with black lowest and red highest, but in this case all are ~ 0.8 – 1 . The best-fitting value and errors for cloud 1 are shown (black line and grey shading).

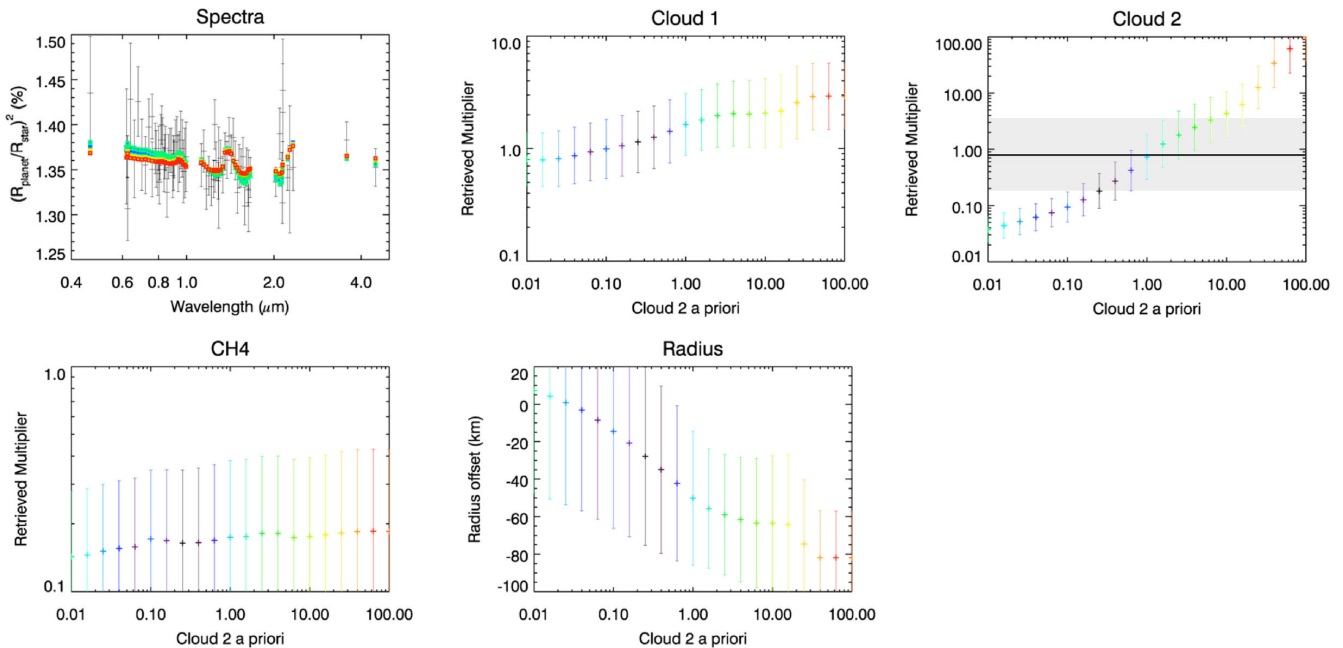


Figure 5. Bracketed retrieval results for GJ 1214b, where the a priori being altered is the cloud 2 number density. We do not plot the results for H₂O or CO₂ as the retrieved values do not vary significantly for different a priori scenarios. The different colours correspond to different values of the reduced χ^2 , with black lowest and red highest, but in this case all are ~ 0.8 . The best-fitting value and errors for cloud 2 are shown (black line and grey shading).

other properties, so there is currently no evidence for its presence on GJ 1214b.

The only variable we can place any constraint on is the CH₄ VMR, where the retrieved VMR is above 20 \times the a priori, equivalent to 1 per cent, the reduced χ^2 is significantly higher (Fig. 8), so we can place a tentative upper limit of 1 per cent on the CH₄ abundance in GJ 1214b’s atmosphere, within the limitations of our model scenario. However, this is not a very stringent constraint, and we

conclude that at present there is not enough information in the data to reliably constrain GJ 1214b’s atmosphere, and we do not claim to have detected either cloud or molecular features in the spectrum.

5 DISCUSSION

It is clear from the results presented in Section 4 that the retrieval is heavily dependent on the a priori assumptions in our atmospheric

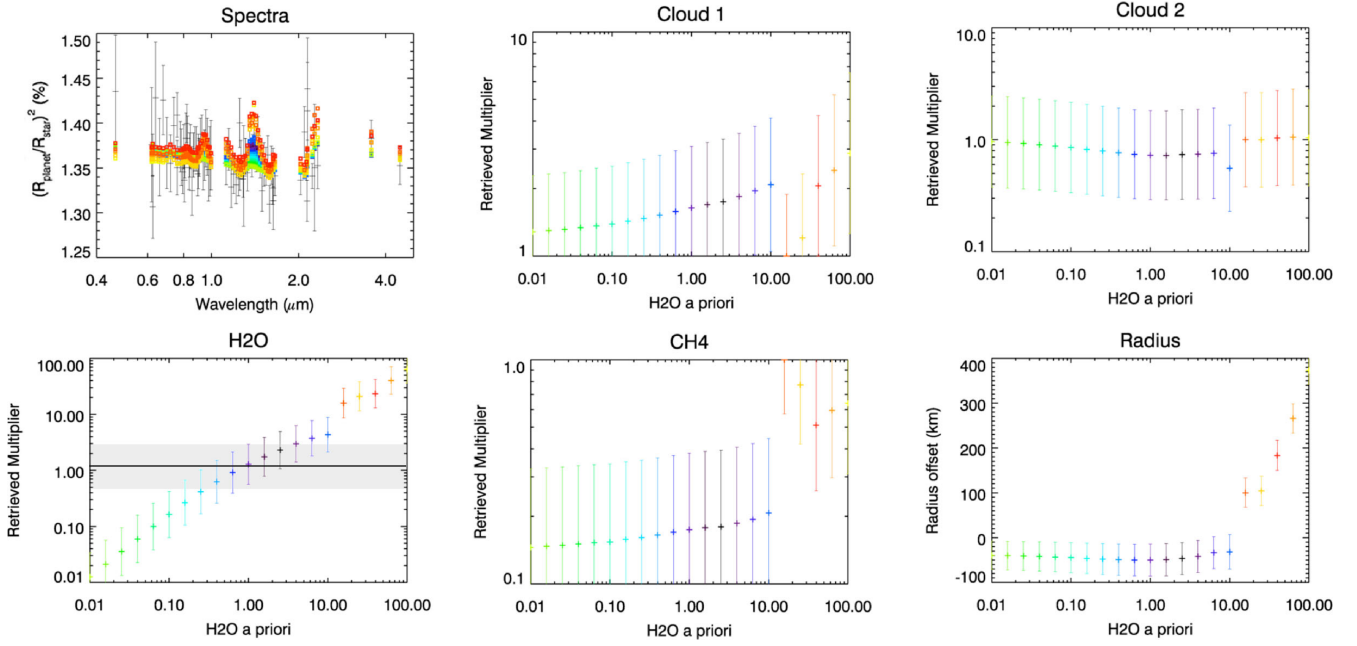


Figure 6. Bracketed retrieval results for GJ 1214b, where the a priori being altered is the H₂O VMR. We do not plot the results for CO₂ as the retrieved values do not vary significantly for different a priori scenarios. The different colours correspond to different values of the reduced χ^2 , with black lowest and red highest, but in this case all except the rightmost five points are ~ 0.8 ; those five points are between 1.0 and 1.46. The best-fitting value and errors for H₂O are shown (black line and grey shading).

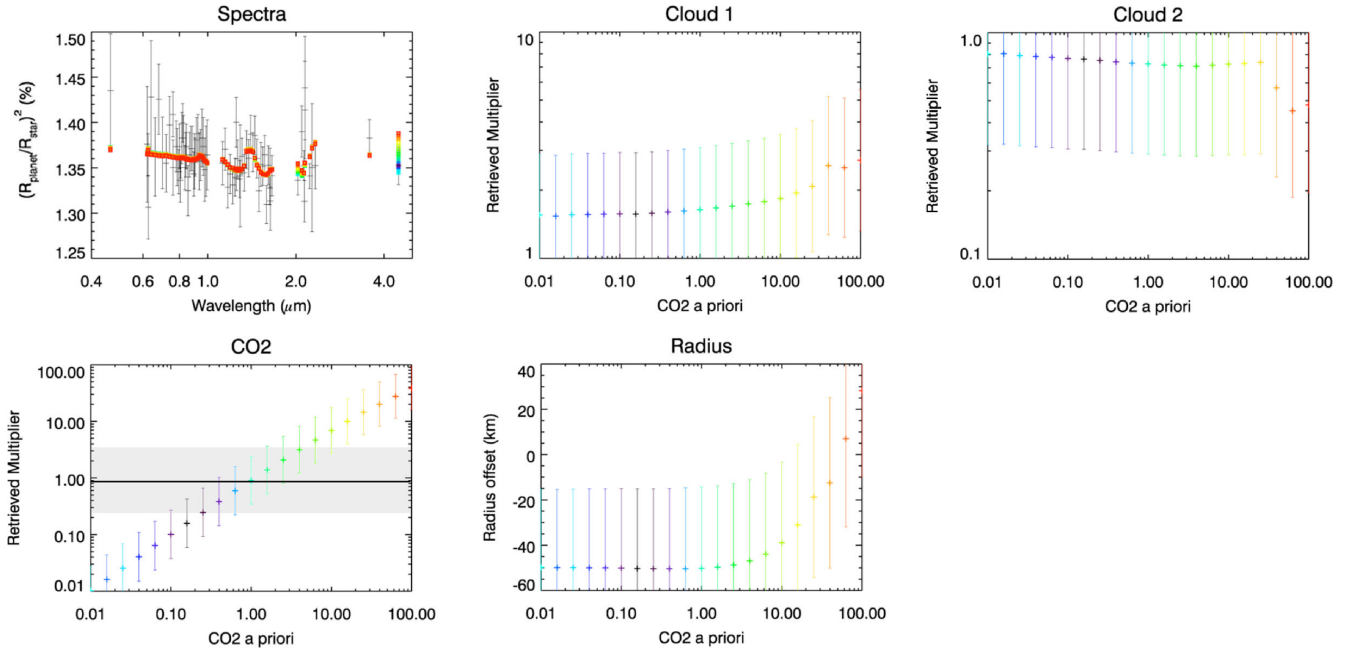


Figure 7. Bracketed retrieval results for GJ 1214b, where the a priori being altered is the CO₂ VMR. We do not plot the results for H₂O and CH₄ as the retrieved values do not vary significantly for different a priori scenarios. The different colours correspond to different values of the reduced χ^2 , with black lowest and red highest, but in this case all are ~ 0.8 . The best-fitting value and errors for CO₂ are shown (black line and grey shading).

model, and therefore we can arrive at no firm conclusion about the nature of GJ 1214b's atmosphere. We have shown that it is possible to produce a good fit to the full visible and infrared spectrum with a cloudy H₂–He atmosphere, but it is important to understand the implications of the assumptions that went into this model. We present a series of further retrieval tests below, in which we have altered

some of the non-retrieved model parameters/data to investigate their influence on the result. Whilst these tests do not shed any further light on GJ 1214b's atmospheric composition at this time, in order for retrieval methods to fully exploit any future measurements it is crucial that we understand the sensitivities of the spectrum to the model parameters.

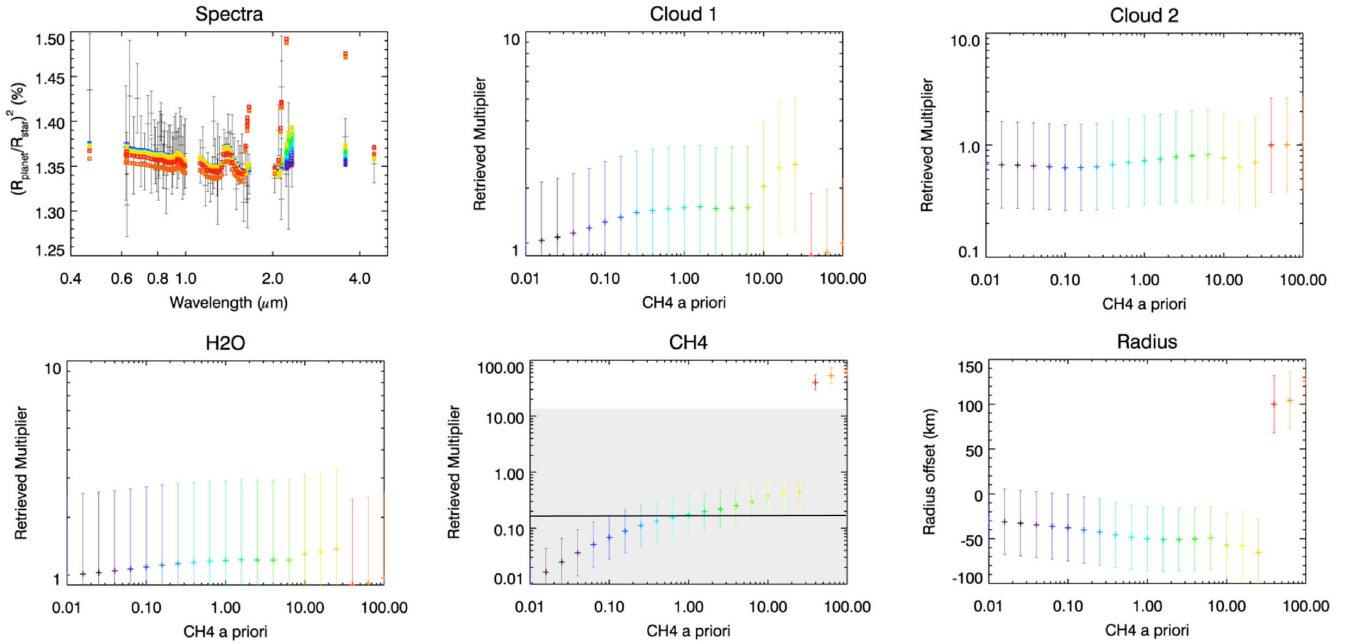


Figure 8. Bracketed retrieval results for GJ 1214b, where the a priori being altered is the CH₄ VMR. We do not plot the results for cloud 2 and CO₂ as the retrieved values do not vary significantly for different a priori scenarios. The different colours correspond to different values of the reduced χ^2 , with black lowest and red highest, but in this case all are ~ 0.8 except the rightmost three points in the plots, which are ~ 4 . The best-fitting value and errors for CH₄ are shown (black line and grey shading).

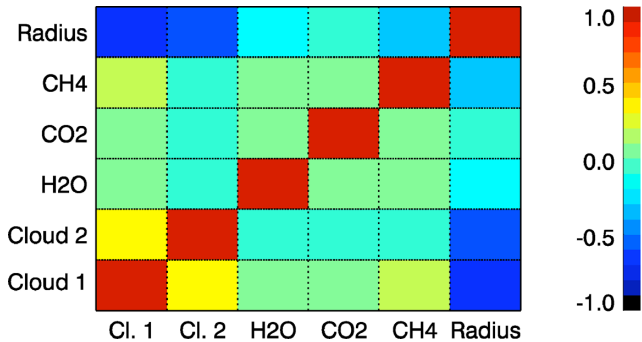


Figure 9. The correlation matrix for this retrieval problem. A correlation of +1 indicates perfect positive correlation, -1 perfect negative correlation. There is significant negative correlation between radius and all the other variables except H₂O and CO₂ VMR. There is significant positive correlation between cloud 1 number density and cloud 2 number density, and CH₄ VMR.

5.1 Data usage

Since this work commenced, further observations of GJ 1214b have been published, most notably those of Fraine et al. (2013); these authors have repeated the warm *Spitzer* 3.6 and 4.5 μm measurements of Désert et al. (2011), and whilst the radii are not incompatible with those previously derived the errors are somewhat smaller. This may result in the *Spitzer* points providing further constraint on the model atmosphere, so we repeat the above analysis including the Fraine et al. (2013) points instead of the Désert et al. (2011) points. This produced a small (<10 per cent) difference in the values of all best-fitting model parameters except the CO₂ and CH₄ VMRs, with the CO₂ multiplier reduced to $0.682 \pm 1.10 \times$ from $0.876 \times$ the a priori VMR and CH₄ increased to $0.237 \pm 0.54 \times$ from $0.169 \times$. However, this variation is well within the retrieval error.

We did not test the inclusion of the Fraine et al. (2013) Iz (0.8–1.1 μm) point, since it is compatible with existing measurements in the wavelength region and we felt it was unlikely that any information would be added.

As mentioned in Section 2, combining data at different wavelengths from multiple sources is often problematic in transmission spectroscopy, because of temporal changes in stellar activity and also different instrument systematics/processing techniques from different observations. In our original analysis, we have attempted to account for this by increasing the error bars on some measurements to ensure that measurements obtained in the same wavelength region are in agreement within their error bars. To test the impact of this, we repeated the analysis with the published errors. We also performed the same analysis with only the spectroscopic data sets (VLT/FORS blue and red, *HST*/WFC3 and Magellen/MMIRS *K* band) plus the *Spitzer*/IRAC measurements, since the ground-based photometric data points are seen to be the most discrepant (Fig. 1) and are also the most difficult to match with data at different wavelengths obtained at different times; it is extremely challenging to absolutely calibrate the out-of-transit baseline for atmospheric effects, adding to the uncertainty on the transit radius for single photometric points relative to other data sets. This test also used the published errors.

We performed two additional tests for the spectroscopic data plus *Spitzer*; to check the sensitivity of the result to shifts in the baseline radius for different data sets, we shifted the FORS blue points down by the same amount as Bean et al. (2011). We also shifted the FORS red points up by the same amount in a separate test. The average best-fitting retrieved values and errors are shown for each of these test cases in Table 5.

It can be seen in Table 5 that the variation in the average best-fitting retrieved values is well within the error bounds on those values. The behaviour of the bracketed retrieval is also robust under the different combinations and treatments of the data, as the same

Table 5. The parameter values in the best-fitting models for five different treatments of the available data.

Variable	Original	Pub. errors	Spectroscopic	FORS blue down	FORS red up
Cloud 1	1.55 ± 1.00	1.38 ± 0.93	1.69 ± 0.90	1.60 ± 1.00	1.73 ± 0.892
Cloud 2	0.783 ± 1.13	0.704 ± 1.10	0.504 ± 1.22	0.743 ± 1.13	0.489 ± 1.22
H ₂ O VMR	1.16 ± 1.04	1.00 ± 1.05	0.980 ± 1.01	1.27 ± 1.03	0.972 ± 1.01
CO ₂ VMR	0.876 ± 1.16	0.879 ± 1.17	0.838 ± 1.12	0.856 ± 1.14	0.833 ± 1.12
CH ₄ VMR	0.169 ± 0.732	0.199 ± 0.782	0.174 ± 0.689	0.199 ± 0.737	0.175 ± 0.694
10-bar radius	15320 ± 58 km	15345 ± 58 km	15340 ± 53 km	15327 ± 57 km	15342 ± 54 km

correlations between variables and dependence on the a priori seen in Figs 4–8 are reproduced in all cases. The only difference is that the reduced χ^2 is somewhat higher for the published error case, at ~ 1.5 . Our result, namely that the existing data are non-constraining, is therefore not dependent on the details of the data sets chosen or the treatment of the error bars on those data sets. For future analyses of this kind, in which spectroscopic features can be resolved with a reasonable signal-to-noise ratio, a more detailed approach would be necessary. An appropriate technique would be to create a grid of offsets between different data sets, and then to run the retrieval for all cases to examine the effect on the result of any unknown systematic errors. This could be extended to also include variable gradients for visible data, which are the most likely to be affected by the presence of star spots. We stress that the error budget for spectroscopic measurements that are combined in this way is likely to be dominated by systematics, so any conclusive result must involve rigorous testing of the kind described in order to ensure its robustness. However, since we cannot draw any firm conclusions from the existing GJ 1214b data, it is clear that further testing would serve no purpose in this case.

5.2 Cloud altitude

In the previous section, we retrieved the cloud particle abundances for both cloud modes, but we did not allow the altitude of the cloud to vary. In transmission geometry, the cloud top altitude is most important because the long slant path through the cloud means that it quickly becomes optically thick deeper in the atmosphere. We adjusted the cloud top pressures to 0.1 mbar and 10 mbar from the a priori of 1 mbar and repeated the retrieval analysis for these cases. A good fit to the data can be obtained for all of these cloud top pressures, and the best-fitting parameter values for each pressure are shown in Table 6.

The effect of changing the cloud top altitude on the results can clearly be seen, and for the most part is straightforward to understand. Decreasing the cloud top pressure and increasing the altitude mean that gas absorption features are truncated at higher altitudes, so abundances must increase in order to fit the size of the observed features, and the radius at 10 bars is smaller because the higher cloud

Table 6. The parameter values in the best-fitting models for three different cloud top pressures, expressed as multiplying factors on the model values listed in Table 2 except for the radius which is in km.

Variable	10 mbar	1 mbar	0.1 mbar
Cloud 1	0.981 ± 1.16	1.55 ± 1.00	0.530 ± 0.867
Cloud 2	0.301 ± 1.59	0.783 ± 1.13	0.162 ± 1.25
H ₂ O VMR	0.522 ± 0.788	1.16 ± 1.04	1.75 ± 1.11
CO ₂ VMR	0.619 ± 1.00	0.876 ± 1.1	0.971 ± 1.17
CH ₄ VMR	0.0575 ± 0.432	0.169 ± 0.732	0.219 ± 0.841
10-bar radius	15515 ± 27 km	15320 ± 58 km	15224 ± 97 km

increases the radius of atmospheric extinction. The opposite is true when the cloud top pressure is increased/altitude is decreased. Less intuitively, the cloud abundances decrease if the cloud top pressure is either lowered or raised, indicating the complexity of the degeneracy between different scenarios; for example, the CH₄ VMR is very low for the 10 mbar case, so the features appear to be the same size despite both a lower cloud top and a lower abundance. It is clear that degeneracies allow compensation between the model parameters such that a reasonable fit to the data can be achieved regardless of the position of the cloud top.

These results indicate that different assumptions about the vertical distribution of cloud have an effect on retrieval results; the most significant effect is on the cloud 2 abundance, which varies by a factor of 5 if the cloud top is moved from 1 mbar to 0.1 mbar. With the current quality of data we cannot expect to achieve better retrieval precision than this anyway, but when the data are more constraining this kind of degeneracy will limit our ability to draw firm conclusions about GJ 1214b. A comparison between retrieval results and *ab initio* models could allow differentiation between degenerate atmospheric scenarios on the basis of physical likelihood.

5.3 Temperature profile

Whilst there is insufficient information in the spectrum to retrieve the atmospheric temperature, the atmospheric scale height is proportional to temperature so it will have some effect on the spectrum. We test this by repeating the retrieval with our input temperature profile shifted by -50 and $+50$ K. As in Section 5.2, we present the best-fitting parameter values from each case in Table 7. The lower temperature profile tested here corresponds to an equilibrium temperature of 480 K and a Bond albedo of 0.5 in our simple temperature profile model, which may be a likely scenario if the planet's albedo is dominated by scattering from a high, reflective cloud layer.

A decrease in temperature decreases the atmospheric scale height, which also decreases the radius of the atmosphere above the 10 bar pressure level. The 10-bar radius and cloud opacities therefore increase to counteract this effect. A decreased scale height also makes gaseous absorption features appear to be flatter, so the gas VMRs are increased to compensate for this. The opposite is true

Table 7. The parameter values in the best-fitting models for three different atmospheric temperatures, as Table 6.

Variable	-50 K	$+0$ K	$+50$ K
Cloud 1	2.06 ± 0.97	1.55 ± 1.00	1.11 ± 0.985
Cloud 2	0.813 ± 1.17	0.783 ± 1.13	0.591 ± 1.12
H ₂ O VMR	1.39 ± 1.07	1.16 ± 1.04	0.882 ± 0.947
CO ₂ VMR	0.94 ± 1.18	0.876 ± 1.16	0.76 ± 1.09
CH ₄ VMR	0.217 ± 0.634	0.169 ± 0.732	0.125 ± 0.656
10-bar radius	15455 ± 52 km	15320 ± 58 km	15190 ± 59 km

when the temperature is increased. A very similar effect to that for a temperature decrease would be observed if the mean molecular weight of the atmosphere was increased by the addition of a heavier spectrally inactive gas such as N_2 .

As in Section 5.2, changing the model temperature profile has a non-negligible effect on the retrieved parameters, so the radius retrieval alone does not fully compensate for the effect of temperature on the atmosphere scale height. Again, with improved data quality and better constraints this inherent degeneracy will become more important. It will therefore be essential to observe a secondary transit of GJ 1214b in the future, as this could provide further information about the temperature structure of the atmosphere.

5.4 H₂O-dominated atmospheres

We have not considered in detail the possibility of H₂O-dominated atmospheric scenarios, since it has already been shown (Bean et al. 2011; Berta et al. 2012) that a reasonable χ^2 can be achieved with a high molecular weight atmosphere. For completeness, we perform a retrieval with the H₂O VMR set to 0.5, varying the cloud abundances, CO₂/CH₄ VMRs and the radius. A fit can be achieved with a reduced χ^2 of 0.92, for the parameter values in Table 8.

The best-fitting model for the 50 per cent H₂O scenario is shown in Fig. 10. It can be seen that the features do not differ greatly from the best-fitting H₂–He models, except the slight increase in radius

Table 8. The parameter values in the retrieved model for a 50 per cent H₂O atmosphere, as Table 6. The H₂O VMR is set, not retrieved, and a full bracketed retrieval was not performed in this case, so the error is the retrieval error from a single run.

Variable	Retrieved	Error
Cloud 1	2.17	2.13
Cloud 2	0.992	0.992
H ₂ O VMR	500	Fixed
CO ₂ VMR	1.00	1.00
CH ₄ VMR	0.923	0.896
10-bar radius	16 634	18 km

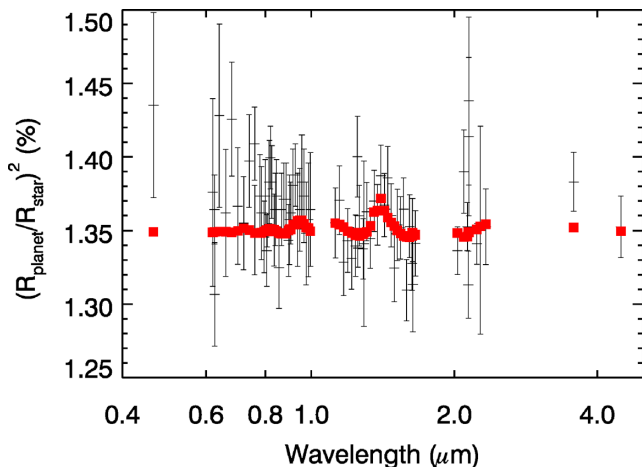


Figure 10. Best-fitting spectrum for GJ 1214b where the H₂O VMR is set to 0.5. The data are shown in black and the model is shown in red.

towards the blue end of the spectrum is no longer seen for a high molecular weight atmosphere. This demonstrates that our method can also produce a good fit to the spectrum for an H₂O-dominated atmosphere, and so despite showing that a cloudy mini-Neptune atmosphere is a strong possibility we cannot rule out the water-world scenario for GJ 1214b.

5.5 Future measurements

The data currently available are sparse and have low signal-to-noise ratio. Future missions such as the *James Webb Space Telescope* and the *Exoplanet Characterisation Observatory (EChO; Tinetti 2012)* will enable the whole near-infrared spectrum to be covered simultaneously at high precision and, in the case of *EChO*, the full spectrum between 0.55 and 16 μm (Fig. 12). In addition, ground-based techniques for transit spectroscopy, particularly those employing multi-object spectroscopy (e.g. Bean et al. 2010; Gibson et al. 2013), are constantly improving. High-dispersion spectroscopy techniques such as that pioneered by Snellen et al. (2010) can provide unambiguous detection of molecular absorbers in exoplanet atmospheres, which will also help to break degeneracies. With higher precision and better coverage, future space- and ground-based observations should enable us to finally distinguish between competing scenarios for this planet, and break some of the degeneracies explored in this paper. We show a range of synthetic spectra for the spectral range and resolution probed by *EChO* to demonstrate this (Fig. 11); clear differences between the scenarios can be seen in the visible, and in CH₄ and CO₂ absorption bands in the infrared. However, spectra with different atmospheric temperature structures are still degenerate even with increased coverage and spectral resolving power, so it would be necessary to observe a secondary transit to fully constrain the properties of the atmosphere.

We investigate whether there is sufficient information to constrain the atmosphere in an *EChO* spectrum by performing the same analysis as that described in Barstow et al. (2013). We take the synthetic spectrum calculated from the best-fitting model atmosphere and add the expected level of Gaussian random noise for an *EChO* observation of GJ 1214b, as shown in Fig. 12. We then feed the noisy spectrum back into NEMESIS to perform a retrieval, as though it was an observed spectrum, and then compare the retrieved parameters with the original model parameters (Table 9). We find that NEMESIS could retrieve the H₂O and CH₄ VMRs from a noisy *EChO* spectrum to within 10 per cent of the input value; the cloud 1 number density is retrieved to within 15 per cent, and all these parameters are retrieved to within 1σ , given correct estimates for the cloud top height and temperature profile. The cloud 2 number density and CO₂ VMR were retrieved correctly to within 2σ .

We perform the same retrieval test with the noisy *EChO* synthetic when the H₂O VMR is forced to be 50 per cent. The retrieved spectrum does not provide as good a fit to the noisy synthetic as the retrieved H₂–He atmosphere spectrum, giving a reduced χ^2 of 2.1 instead of 0.9. The two retrieved spectra are shown overplotted on the noisy synthetic in Fig. 13, and it can be seen that the regions in which they differ most are the visible region, the infrared longwards of 5 μm , and the CH₄ and CO₂ bands at 3.3 and 4.3 μm , respectively. The *EChO* spectrum for GJ 1214b is likely to be too noisy in the visible to distinguish between the models, as demonstrated by comparable reduced χ^2 over the range from 0.55 to 0.95 μm (Table 10), but it is clear that the CH₄/CO₂ bands and especially the mid-infrared region are very useful for distinguishing between the two scenarios with *EChO*. With data of the coverage and quality we expect from a space telescope such as *EChO*, we should be able

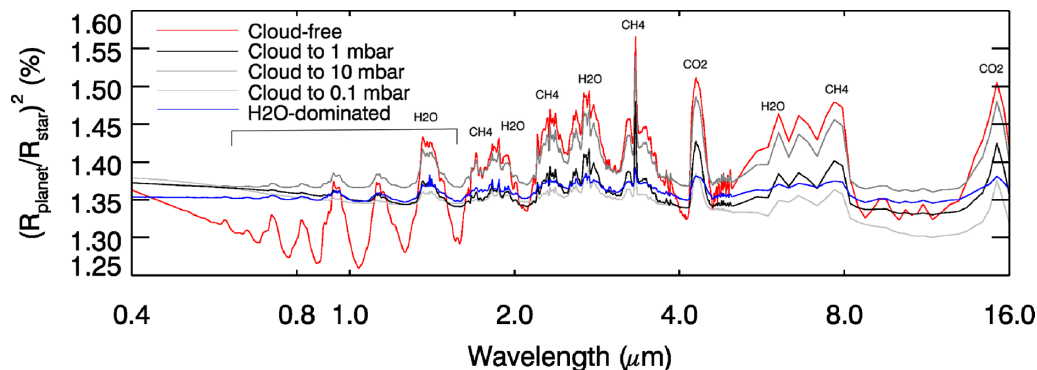


Figure 11. Synthetic spectra between 0.4 and 16 μm for a range of the cases discussed in this paper, with the major gaseous absorption bands indicated. It can be seen that cloudy/cloud-free/water-rich models are very different at short wavelengths, and that the shapes of the CH_4 band at 3.3 μm and the CO_2 bands at 4.3 and 16 μm will also be very important, if these molecules are present in the atmosphere. Spectra for different temperatures are not shown because they are very similar and therefore still degenerate even with greater spectral coverage, so it will be necessary to obtain emission spectra to constrain temperature structure.

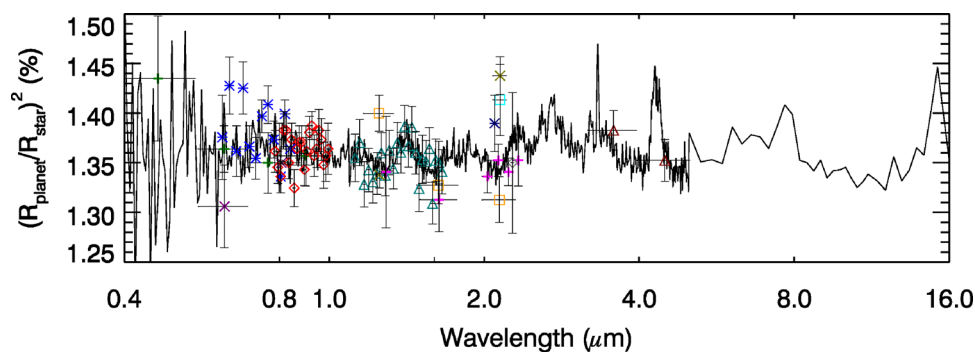


Figure 12. Our best-fitting model spectrum as it would be seen by *EChO*, with the current data also plotted as in Fig. 1. The noisy synthetic has been generated as in Barstow et al. (2013), assuming photon noise and 30 co-added transits. Whereas the faintness of the M dwarf star at short wavelengths means the spectrum is noise-dominated here, the coverage in the infrared would prove very useful.

Table 9. The retrieved parameter values for the synthetic noisy *EChO* spectrum compared with the known input values. The a priori values were all 1.0, with the exception of the radius for which it was 15 455 km.

Variable	Input	Retrieved	Error
Cloud 1	1.55	1.31	0.24
Cloud 2	0.783	1.10	0.25
H_2O VMR	1.16	1.28	0.21
CO_2 VMR	0.876	1.14	0.17
CH_4 VMR	0.169	0.177	0.022
10-bar radius	15 320 km	15 316 km	8 km

to distinguish between the cloudy mini-Neptune and water-world scenarios for GJ 1214b; however, our ability to provide more detailed constraints on the atmosphere is limited by the degeneracies discussed in Sections 5.2 and 5.3.

6 CONCLUSIONS

We have used the NEMESIS radiative transfer and retrieval tool to explore the degeneracy of the retrieval problem for GJ 1214b. We find that the spectroscopic data are compatible with an H_2 -He dominated, cloudy atmosphere. A range of models with 0.1 μm tholin haze particles, 1 μm tholin cloud particles and trace amounts of H_2O , CO_2 and CH_4 produce synthetic spectra that provide a good

fit to the data; however, the number of models with a good fit allows for several orders of magnitude of variation in the abundances of these, so it is difficult to place meaningful constraints. We also cannot rule out the possibility of an H_2O -dominated atmosphere with a small-scale height, as this results in a synthetic spectrum with an equally good fit to the data. In addition, for a cloudy H_2 -He atmosphere the cloud top pressure and temperature profile specified in the model atmosphere significantly affect the retrieved cloud and gas abundances, indicating the presence of further model degeneracy. A disc-integrated emission spectrum from secondary transit will help to constrain the temperature profile, and will be necessary to break these degeneracies.

Future observations will be crucial for finally determining the nature of GJ 1214b. Improvements in the precision of ground-based transit spectra are hoped to provide more conclusive answers, and in the longer term we look to space-based missions such as *EChO*, which should be able to distinguish between H_2 -He- and H_2O -dominated atmospheres. We have demonstrated that NEMESIS is a valuable tool, and our exploration of the degeneracies in this retrieval problem will enable us to find the best approach for the interpretation of future data.

ACKNOWLEDGEMENTS

JKB acknowledges the support of the John Fell Oxford University Press (OUP) Research Fund for this research and LNF is supported

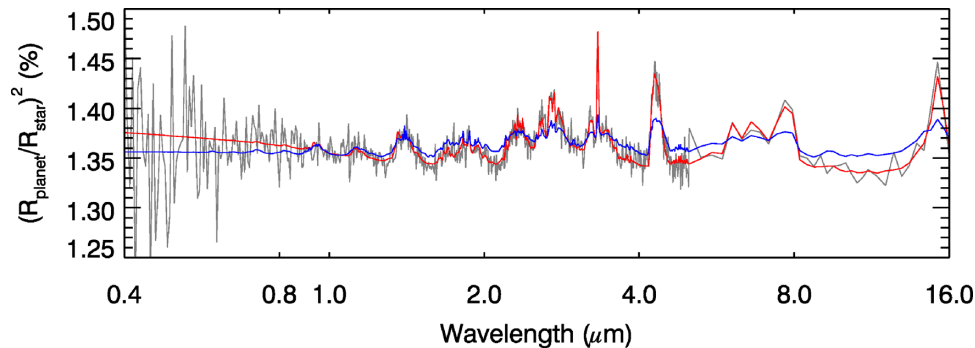


Figure 13. Two retrieval fits to the noisy *EChO* synthetic, with the H₂–He model (red) and a 50 per cent H₂O model (blue). It can be seen clearly that the 50 per cent H₂O model does not produce an adequate fit to a noisy *EChO* synthetic generated with a H₂–He model atmosphere. This indicates that with *EChO* we should be able to distinguish between the two competing scenarios.

Table 10. Reduced χ^2 for different spectral ranges, comparing the fit of the H₂–He model and the 50 per cent H₂O model with the noisy synthetic *EChO* spectrum.

Wavelength (μm)	Reduced χ^2 (H ₂ –He)	Reduced χ^2 (H ₂ O)
0.55–0.95	1.08	1.14
3–5	0.91	2.96
5–11	1.53	8.49
5–16	1.29	7.28
Full	0.90	2.10

by a Royal Society Research Fellowship. We thank the anonymous reviewer for their comments on this paper.

REFERENCES

- Atreya S. K., Wong A. S., Baines K. H., Wong M. H., Owen T. S., 2005, *Planet. Space Sci.*, 53, 498
- Barstow J. K. et al., 2012, *Icarus*, 217, 542
- Barstow J. K., Aigrain S., Irwin P. G. J., Bowles N., Fletcher L. N., Lee J.-M., 2013, *MNRAS*, 430, 1188
- Bean J. L., Miller-Ricci Kempton E., Homeier D., 2010, *Nat*, 468, 669
- Bean J. L. et al., 2011, *ApJ*, 743, 92
- Benneke B., Seager S., 2012, *ApJ*, 753, 100
- Berta Z. K., Charbonneau D., Bean J., Irwin J., Burke C. J., Désert J.-M., Nutzman P., Falco E. E., 2011, *ApJ*, 736, 12
- Berta Z. K. et al., 2012, *ApJ*, 747, 35
- Charbonneau D. et al., 2009, *Nat*, 462, 891
- Cottini V. et al., 2012, *Icarus*, 220, 855
- Coustenis A. et al., 1997, in Soderblom D., ed., *ASP Conf. Ser. Vol. 119. Planets Beyond the Solar system and the Next Generation of Space Missions. Spectroscopy of 51 Peg B: Search for Atmospheric Signatures.* Astron. Soc. Pac., San Francisco, p. 101
- Crisp D., 1986, *Icarus*, 67, 484
- Croll B., Albert L., Jayawardhana R., Miller-Ricci Kempton E., Fortney J. J., Murray N., Neilson H., 2011, *ApJ*, 736, 78
- de Kok R. J., Stam D. M., 2012, *Icarus*, 221, 517
- de Mooij E. J. W. et al., 2012, *A&A*, 538, A46
- Désert J.-M. et al., 2011, *ApJ*, 731, L40
- Fraine J. D. et al., 2013, *ApJ*, 765, 127
- Gibson N. P., Aigrain S., Barstow J. K., Evans T. M., Fletcher L. N., Irwin P. G. J., 2013, *MNRAS*, 428, 3680
- Goody R. M., Yung Y. L., 1989, *Atmospheric Radiation: Theoretical Basis.* Oxford University Press, New York, NY
- Grinspoon D. H., Pollack J. B., Sitton B. R., Carlson R. W., Kamp L. W., Baines K. H., Encrenaz T., Taylor F. W., 1993, *Planet. Space Sci.*, 41, 515
- Harpsoe K. B. W. et al., 2013, *A&A*, 549, A10
- Hawley S. L., Gizis J. E., Reid I. N., 1996, *AJ*, 112, 2799
- Howe A. R., Burrows A. S., 2012, *ApJ*, 756, 176
- Irwin P. G. J. et al., 2008, *J. Quant. Spectrosc. Radiat. Transf.*, 109, 1136
- Irwin J., Charbonneau D., Nutzman P., Falco E., 2009, in Pont F., Sasselov D., Holman M. J., eds, *IAU Symp. Vol. 253. The MEarth Project: Searching for Transiting Habitable super-Earths around Nearby M Dwarfs.* Cambridge Univ. Press, Cambridge, p. 37
- Irwin P. G. J., Teanby N. A., Davis G. R., Fletcher L. N., Orton G. S., Tice D., Kyffin A., 2011, *Icarus*, 212, 339
- Khare B. N., Sagan C., Arakawa E. T., Suits F., Callcott T. A., Williams M. W., 1984, *Icarus*, 60, 127
- Knutson H. A., Charbonneau D., Allen L. E., Burrows A., Megeath S. T., 2008, *ApJ*, 673, 526
- Kundurthy P., Agol E., Becker A. C., Barnes R., Williams B., Mukadam A., 2011, *ApJ*, 731, 123
- Lacis A. A., Oinas V., 1991, *J. Geophys. Res.*, 96, 9027
- Lee J.-M., Fletcher L. N., Irwin P. G. J., 2012, *MNRAS*, 420, 170
- Lodders K., Fegley B., 2002, *Icarus*, 155, 393
- Miller-Ricci E., Fortney J., 2010, *ApJ*, 716, L74
- Miller-Ricci Kempton E., Zahnle K., Fortney J. J., 2012, *ApJ*, 745, 3
- Morley C. V., Fortney J. J., Marley M. S., Visscher C., Saumon D., Leggett S. K., 2012, *ApJ*, 756, 172
- Morley C. V., Fortney J. J., Kempton E. M.-R., Marley M. S., Visscher C., 2013, *ApJ*, preprint (arXiv:1305.4124)
- Murgas F., Pallé E., Cabrera-Lavers A., Colón K. D., Martín E. L., Parviainen H., 2012, *A&A*, 544, A41
- Narita N., Nagayama T., Suenaga T., Fukui A., Ikoma M., Nakajima Y., Nishiyama S., Tamura M., 2012, *PASJ*, 65, 2
- Pollack J. et al., 1993, *Icarus*, 103, 1
- Pont F., Sing D. K., Gibson N. P., Aigrain S., Henry G., Husnoo N., 2013, *MNRAS*, 432, 2917
- Rodgers C. D., 2000, *Inverse Methods for Atmospheric Sounding.* World Scientific Press, Singapore
- Rothman L. S. et al., 2010, *J. Quantit. Spectrosc. Radiat. Transfer*, 111, 2139
- Seager S., Sasselov D. D., 2000, *ApJ*, 537, 916
- Sing D. K., Vidal-Madjar A., Désert J.-M., Lecavelier des Etangs A., Ballester G., 2008, *ApJ*, 686, 658
- Snellen I. A. G., de Kok R. J., de Mooij E. J. W., Albrecht S., 2010, *Nat*, 465, 1049
- Swain M. R., Vasisht G., Tinetti G., Bouwman J., Chen P., Yung Y., Deming D., Deroo P., 2009, *ApJ*, 690, L114
- Tashkun S. A., Perevalov V. I., Teffo J.-L., Bykov A. D., Lavrentieva N. N., 2003, *J. Quantit. Spectrosc. Radiat. Transfer*, 82, 165
- Tinetti G. et al., 2012, *Exp. Astron.*, 34, 311
- Tsang C. C. C. et al., 2010, *Geophys. Res. Lett.*, 37, 2202
- Wenger C., Champion J. P., 1998, *J. Quantit. Spectrosc. Radiat. Transfer*, 59, 471